Article:
Ramadhan, AA orcid.org/0000-0002-0711-572X, Kapur, N, Summers, JL et al. (1 more author) (2017) Numerical modelling of electrohydrodynamic airflow induced in a wire-to-grid channel. Journal of Electrostatics, 87. pp. 123-139. ISSN 0304-3886

https://doi.org/10.1016/j.elstat.2017.04.004

Numerical modelling of electrohydrodynamic airflow induced in a wire-to-grid channel

Abdulmajeed A. Ramadhan[a,b,*], N. Kapur[a], J.L. Summers[a], H.M. Thompson[a]

[a] School of Mechanical Engineering, University of Leeds, UK.
[b] Department of Mechanical Engineering, University of Anbar, Iraq.

Abstract

Electrohydrodynamic (EHD) airflows provide a means of generating air motion by a gas discharge across two electrodes without the need for moving parts. A two-dimensional numerical model for a wire-to-grid EHD air blower is developed, validated against previous data, and used to investigate the influence of key design parameters on blower efficiency, including the emitter wire diameter, the blower height, the locations of the collecting surfaces and grid wires, and the collecting grid density. The optimal locations of both collectors from the corona wire are determined based on blower efficiency at a fixed operating power, resulting in improvements in the average outlet velocity between 9% and 15%, depending on blower thickness. The presence of the grid has a strong influence on the electric field distribution and increases the blower performance, with higher flow, lower operating voltage and reduced blower size. An investigation into the effect of grid density reveals that using coarse collecting grids is generally beneficial, leading to higher efficiency with lower pressure losses.

Keywords: Electrohydrodynamic (EHD) airflow, EHD air blower, design parameters, thermal management.

* Corresponding author.
School of Mechanical Engineering, University of Leeds, UK.
E-mail addresses: mnaarr@leeds.ac.uk , aar7sh@uoanbar.edu.iq (A. Ramadhan).

1. Introduction

Due to its low cost and availability, air remains a widely used cooling medium in many important thermal management applications, including engine and turbine blades in the aerospace industry and a wide range of vehicle heat exchangers in the automotive industry [**1**]. The required cooling from a surface is usually achieved by convective heat transfer to air, whose motion is either generated passively (via thermal gradients) or through the continual input of energy to create a moving air stream. Despite a number of promising innovations using liquid on-chip cooling, Aquasar (IBM) [**2**], and dielectric liquid immersion technology [**3**], convective heat transfer to air as it flows over a heat sink is also still the most common cooling method for microelectronics. In such cases, the air is usually pumped over the hot electronic components by conventional rotary fans, where fan speeds are controlled to maintain appropriate CPU temperatures [**4**, **5**]. However, increased heat generation in microelectronic devices and the demand for ever smaller portable devices, where the performance of rotary fan-based cooling

technology degrades as device dimensions reduce, has led to a critical need for efficient, compact thermal modules that provide acceptable acoustic levels, good reliability and high cooling density [**6-8**].

Wang et al. [**7**] recently compared the performance of a number of alternative air pumping methods for microelectronics cooling, including piezoelectric fans, synthetic jets and electrohydrodynamic (EHD) air pumps. They concluded that although piezoelectric fans and synthetic jets are potentially useful for cooling of localized hot-spots, they are generally unsuitable for consumer electronics due to their inability to generate sufficient air through the electronics they are cooling. In contrast, they found that EHD air movers offer important advantages over rotary fans due to their silent operation, reduced energy consumption, smaller volume requirements, and higher heat transfer performance on small form factor electronics.

EHD air pumps (also known as Electrostatic Fluid Accelerators) convert electrical energy into kinetic energy of the moving air stream by applying a high voltage electric field between a sharp electrode and a grounded surface in the air. This leads to ionization of air molecules, which are then accelerated by the electrostatic forces to create a moving air stream known as an ionic wind (also referred to as a corona or an electric wind). The ionic wind is not a new phenomenon and it was first reported by Francis Hauksbee in 1709 [**9**]. In the mid twentieth century, the basic theory of EHD pumps was developed, and the mechanism of gas movement under the ionic wind effect was investigated by Stuetzer [**10**] and Robinson [**11**]. The latter showed that the gas velocity depends linearly on the applied voltage and varies with the square root of the current. Although Marco and Velkoff [**12**] presented the first comprehensive investigation of the potential of EHD air pumps for convective heat transfer in 1963, and this has been extended by a number of studies subsequently [**13-17**], it is only in the last decade or so that it has received attention as a potential alternative to rotary fans in microelectronics cooling. EHD air pumps were also investigated as secondary flow generators in the presence of the bulk airflow to disrupt the thermal boundary layer for heat transfer enhancements [**18-21**].

A number of recent studies have investigated the effect of various design parameters affecting the emitter-to-electrode configuration on the efficiency of, and convective heat transfer generated by, EHD air pumps. Kalman and Sher [**22**] were the first to investigate the effectiveness of an optimized electrostatic blower, and explore its possibility to be used as a cooling system for electronic components in thermal management applications. The EHD blower consisted of a positively charged wire electrode, 0.5 mm in diameter, stretched between two grounded inclined wings located over a heated plate. They found that the optimized EHD blower can enhance the heat transfer by a factor of more than twofold compared with free convection mechanism. This study was later extended by Rashkovan et al. [**23**] with a wire electrode diameter reduced from 0.5 mm to 0.2 mm to increase the strength of the electric field and resulted in a 50% increase in the heat transfer rate over the previous EHD device. Moreau and Touchard [**24**] later presented a comprehensive investigation into the ionic wind speed induced by a needle emitter

through a tube, considering the effect of voltage polarity and collecting electrode geometry (both grid and ring configurations) as well as electrode gap and tube diameter. They found that generally the ionic wind speeds produced by a positive corona are larger than with a negative one and that using a grid as a collecting electrode is more efficient than a ring; they also found that the grid density has an important influence on ionic wind generation.

Very recently, Tsubone et al. [**25**] and Fylladitakis et al. [**26**] presented experimental and numerical studies to explore the benefits of design optimization of EHD air pumps. The former used a design based on a partially covered wire to parallel plates channel and explored the effect of channel width, the number of emitter wire electrodes and the distance between the emitter wires on both the ionic wind velocity and corona current. Their results demonstrated ample scope for design optimization in order to maximize air speed, flow rate and mechanical power per corona input power. Fylladitakis et al. [**26**] considered the optimization of an EHD air pump for cooling high-power electronics by varying electrode gap and collecting grid density parameters for two EHD air pump prototypes of multi needle-to-grid and multi wire-to-grid configurations. Experimental results of the final optimal configuration demonstrated that the fabricated EHD air pump offered promising performance for practical applications. The first practical and successful integration of an EHD air pump into a real-world electronic application has been performed by Jewell-Larsen et al. in 2009 [**6**], with replacing the conventional fan of a high performance laptop by a retrofitted EHD cooling system. The EHD air pump exhibited a promising cooling performance with lower installation size and acoustic level, compared to the traditional fan.

The numerical modelling of the corona discharge and the resulting ionic wind has been performed by many studies and successfully validated against experimental findings [**18**, **19**, **27**-**29**]. Due to the wide range of the geometrical parameters that strongly affect the discharge process and the performance of the EHD airflow devices, numerical studies offer a great potential to explore various design parameters and save cost and time. The motivation of this work is based on the ongoing attention to improve the EHD flow technology to be an applicable cooling solution for advanced microelectronics. Design optimization is one of the critical factors that determine the performance of the EHD systems to be adopted for thermal management of real world applications. In this paper, a two-dimensional numerical model of a wire-to-grid EHD channel configuration is developed and validated using a finite element based method (employing COMSOL Multiphysics) against a range of experimental and numerical data. Based on thermal management requirements and from a design perspective, a comprehensive investigation and analysis into the influence of several geometrical parameters on the EHD blower efficiency is performed and an optimal configuration is proposed. These parameters are studied for different blower heights and include the emitter wire diameter, the electrode gap between the emitter and the grid, the collector location at the blower walls, and the collecting grid density.

2. Numerical Modelling

2.1 EHD governing equations

The electric field intensity, $\vec{E}$, and the electric potential, V, are defined by Poisson's equation as,

$$\vec{\nabla}.\vec{E} = \nabla^2 V = -\frac{q}{\varepsilon_0} \quad (1)$$

where q is the space charge density (C/m^3) and ε_0 is permittivity of free space (= 8.854×10^{-12} C/V.m).

The charge transport equation that couples the electrostatic and Navier-Stokes equations for the airflow is derived by combining the following three equations:

i. The electric current density equation,

$$\vec{J} = \mu_p \vec{E} q + \vec{U} q - D\,\vec{\nabla} q \quad (2)$$

where μ_p is the air ion mobility in the electric field (m^2/V.s), $\vec{U}$ is the velocity vector of airflow, and D is the diffusivity coefficient of ions (m^2/s).

The three terms on the right side of Eq. (2) represent the charge conduction (the ion movement due to the electric field), charge convection (transport of charges by the airflow), and charge diffusion, respectively [**30**].

ii. The continuity equation for electric current,

$$\vec{\nabla}.\vec{J} = 0 \quad (3)$$

iii. The conservation of mass equation,

$$\vec{\nabla}.\vec{U} = 0 \quad (4)$$

Combining equations (2) and (3) and using the continuity equation (4) gives the charge transport equation,

$$\vec{\nabla}.\left(\mu_p \vec{E} q - D\,\vec{\nabla} q\right) + \vec{U}.\vec{\nabla} q = 0 \quad (5)$$

Since the value of the air velocity ($\vec{U}$), which represents the convection term in Eq. (5), is very small compared with the drift velocity of ions ($\mu_{\mathrm{p}}\vec{E}$) in the conduction term, it can be neglected [**31**].

The Navier-Stokes equations and continuity equation (Eq. 4) describe the fluid dynamic part of the model for steady state incompressible airflow under the effect of the electrostatic force,

$$\rho\vec{U}\,.\,\vec{\nabla}\vec{U} = -\vec{\nabla}p + \mu\nabla^2\vec{U} + q\vec{E} \tag{6}$$

where ρ is the air density (kg/m^3), p is the air pressure (Pa), μ is the air dynamic viscosity (Ns/m^2), and $q\vec{E}$ represents the body or Coulomb force (N/m^3).

2.2 Space charge generation

The gap between the corona and collecting electrodes can be divided into ionization and drifting regions. The space charge density in the ionization zone can be neglected as it contains a mix of electrons and positive ions at similar magnitudes, compared to the drift zone, which contains ions of a single polarity and neutral air molecules. For the positive corona at standard air conditions, the electric field strength E_{e} created on a smooth surface of the corona wire can be estimated by Peek's empirical formula [**32**],

$$E_{\mathrm{e}} = E_0\,(1 + (0.0262\,/\sqrt{R_{\mathrm{e}}})) \tag{7}$$

where R_{e} is the corona wire radius (m), and E_0 is the breakdown electric strength of air (V/m). The boundary conditions for space charge density can be obtained by applying Kaptsov's assumption at the external surface of the ionization zone, which suggests that the electric field increases proportionally to the applied voltage below the corona onset level, but will preserve its value after the corona is initiated [**33**]. In the present numerical simulation, following [**27**], it is assumed that the ionization zone is small enough to be neglected. Under this assumption, the space charge resulting from corona discharge can be estimated by assuming that the electric field strength created at the surface of the corona wire due to the applied voltage is equal to that obtained from Eq. (7).

3. Validation of the numerical method

3.1. Solution domain and boundary conditions

The experimental data and the numerical results of a wire-to-grid EHD channel presented by Jewell-Larsen et al. [**27**] were used to validate the numerical method used in this paper. The EHD channel

geometry mainly consists of a wire emitter electrode, a collecting grid of parallel wires, and collecting channel walls, as shown in **Fig. 1**. A conductive wire is used as a corona electrode and located mid-way between two conductive plates that represent both the collecting electrodes and channel walls. In order to minimize the solution computation time, a symmetry boundary condition is applied at the horizontal plane centered between the channel walls. The coupled equations of the electric field (Eq. 1), the charge transport (Eq. 5), and the airflow (Eqs. 4 and 6), were solved in the half domain using the commercial package, COMSOL Multiphysics (V5.1), with the modelling parameters displayed in **Table 1**.

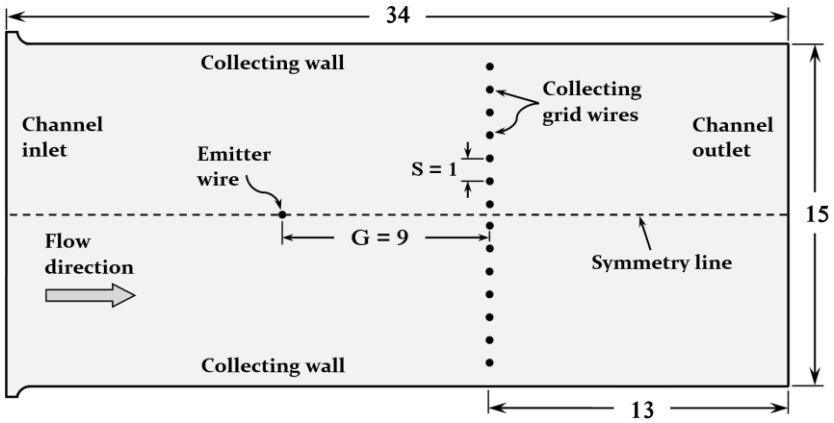

Fig. 1. The numerical simulation domain of the EHD wire-to-grid channel geometry considered in [27]. Dimensions in millimetres.

Table 1. Numerical modelling and geometric parameters used in the model of [27] and in the present validation.

Parameter	Value
Applied potential, V_e	5 – 8 kV
The breakdown electric strength of air, E_0	3.31 ×10^6 V/m
Charge diffusion coefficient, D	5.3 ×10^{-5} m^2/s
Ion mobility coefficient, μ_p	1.8 ×10^{-4} m^2/V.s
Density of air, ρ	1.23 kg/m^3
Dynamic viscosity of air, μ	1.8 ×10^{-5} N.s/m^2
Corona wire to collecting grid distance, G	9 mm
Corona wire radius, R_e	0.05 mm
Collecting grid wire electrode radius	0.05 mm
Number of collecting grid wires	14
Spacing between grid wires, S	1 mm
Channel height	15 mm
Channel length	34 mm
Channel width and corona wire length	277 mm

The modelling equations were solved using the solution procedure shown in **Fig. 2**, subject to the boundary conditions summarized in **Table 2**. The electrostatic mode is modeled with applying a positive potential to the emitter wire surface, while the channel walls and surfaces of all collecting grid wires are grounded with zero volts. For charge transport, a zero diffusive flux condition (Neumann condition) is imposed on all boundaries excluding the surface of the corona wire, where a space charge surface density under an iterated Dirichlet condition is applied [**19**, **31**]. This assumption is based on the fact that the diffusion term is very small compared to the conduction term in Eq. (5), so that its effect on charge

density can be neglected [**31**]. For the flow equations, a standard hydrodynamic boundary condition of no-slip is applied to all solid surfaces of corona electrode, collecting grid wires and channel walls. A zero pressure is applied at the channel outlet, while a normal flow ($v = 0$) with horizontal velocity based on the calculated inlet pressure prescribed from Bernoulli's equation ($u = \sqrt{-2P/\rho}$) is used at the channel inlet [**27**, **29**, **30**]. This assumption is established on the fact that the neutral air particles are accelerated and driven to a certain velocity U_0 under the influence of electrostatic pressure P_e, which is generated in the electric field due to the electrostatic force. Due to the kinetic energy of the gas flow, a stagnation (or dynamic) pressure P_s ($= \rho U_0^2/2$) is created, which is equal to the electrostatic pressure that causes the gas movement [**34**]. Based on this fact, it has been shown experimentally and numerically that the EHD air blower (duct) can be considered to be an ideal pressure source. This is because the cross section of the emitter wire is very small compared to the channel height, and therefore, the flow resistance through the duct can be neglected [**29**].

A mesh independence study was performed by solving the equations on three numerical meshes, with 15122, 22430 and 38350 triangular elements for the half domain, each with high levels of mesh refinement in the regions of high electric field strength (large electric potential gradient) and space charge density, as shown in **Fig. 3**. Results on the two finest grid levels were found to be effectively grid independent since the discrepancies in corona current and average air velocity were approximately 0.1% and 1% respectively. All results presented below have been obtained on the medium grid with 22430 elements.

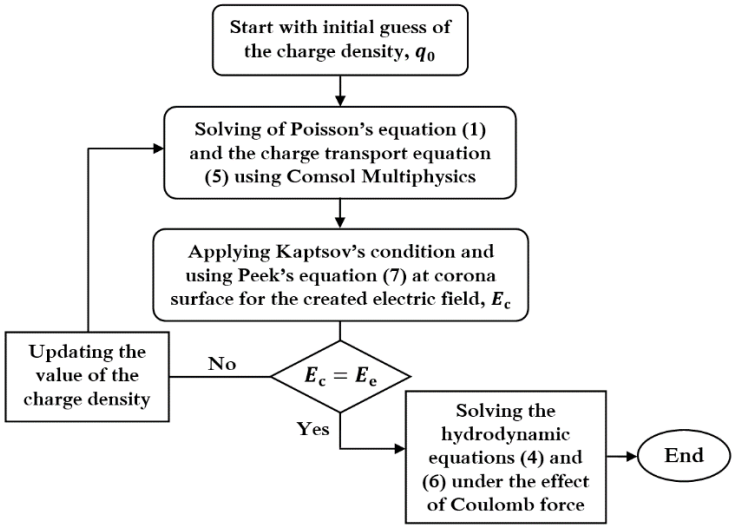

Fig. 2. The numerical solution procedure.

Table 2. Boundary conditions used in the present validation model.

Boundary	Electrostatics	Charge transport	Fluid dynamics
Corona wire electrode	$V = V_e$	Dirichlet condition, $q = q_0$	No-slip ($u = v = 0$)
Channel wall and grid wires	Grounded ($V = 0$)	Dirichlet condition, $q = 0$	No-slip ($u = v = 0$)
Channel inlet	Neumann condition ($\partial V/\partial n = 0$)	Zero diffusive flux ($\partial q/\partial n = 0$)	$u = \sqrt{-2P/\rho}$, $v = 0$
Channel outlet	Neumann condition ($\partial V/\partial n = 0$)	Zero diffusive flux ($\partial q/\partial n = 0$)	$P = 0$
Air boundary	Neumann condition ($\partial V/\partial n = 0$)	Zero diffusive flux ($\partial q/\partial n = 0$)	Symmetry

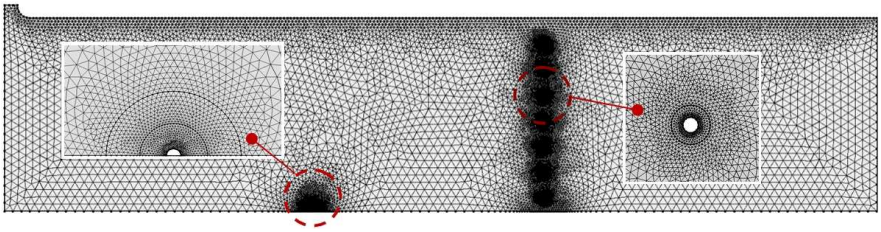

Fig. 3. Distribution of mesh element density of a half computational domain of the wire-to-grid EHD channel geometry, showing the mesh refinement with a high element density around the emitter wire and the collecting surfaces.

3.2 Numerical validation results

Fig. 4 illustrates the results of the numerical solution as surface map distributions generated at 8 kV, for the EHD airflow induced through a wire-to-grid channel considered in [**27**]. The plots agree very well with those presented in [**27**]; they show that the highest space charge density is close the emitter electrode and the air velocity is the largest around the corona wire. Further validation results are shown in **Fig. 5**, which compares current predictions of corona current and air velocity with experimental data and numerical results presented in [**27**], for a range of applied potential. The agreement is also very good in both cases, with maximum discrepancies against the experimental data of 3% and 7% for the corona current and air velocity, respectively, demonstrating the accuracy of the present 2D numerical approach performed using COMSOL Multiphysics.

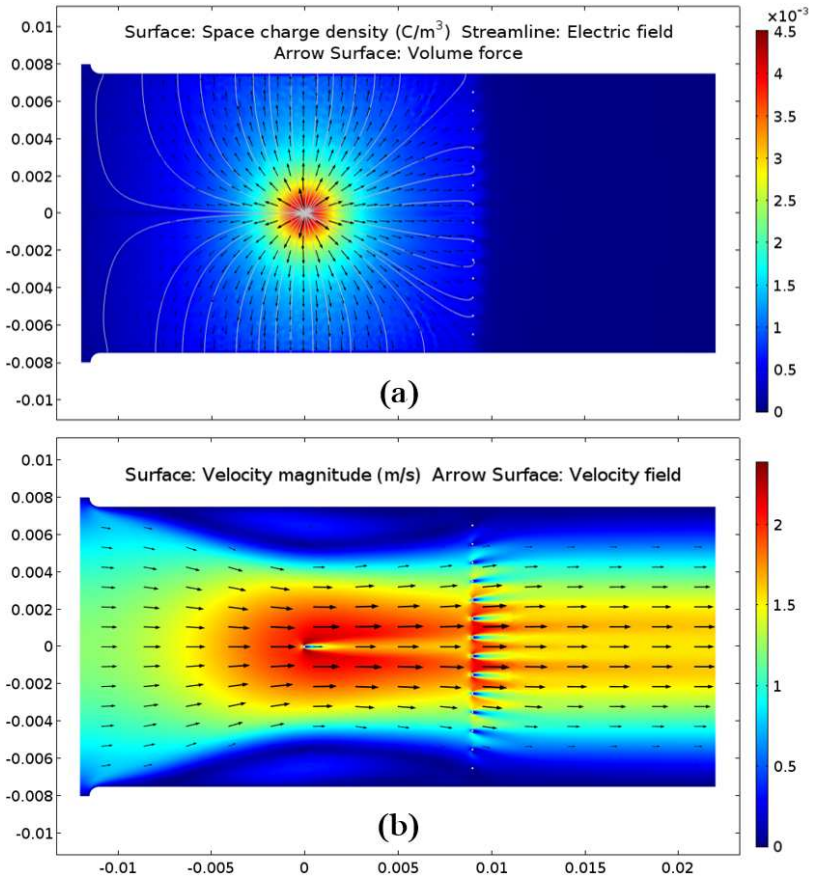

Fig. 4. Numerical validation results in the form of surface map distributions generated at 8 kV: (a) the space charge density with the electric field lines and the body force arrows, and (b) the air velocity. Dimensions in metres.

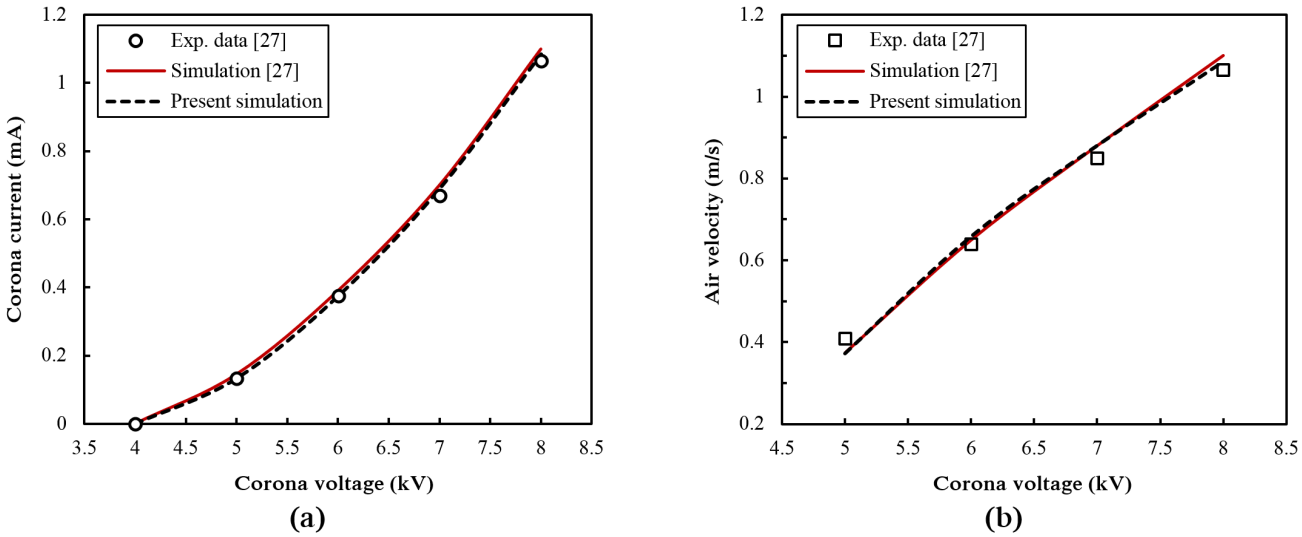

Fig. 5. Comparisons of (a) corona current, and (b) average air velocity at the channel outlet, for a range of corona voltage.

4. Results and discussion

4.1 Numerical configuration domain

The EHD channel geometry used in the present numerical study is shown in **Fig. 6**. It is generally similar to that used in the validation model but with a reduced length of collecting surface located at the channel walls, which is equal to the electrode gap separation between the emitter wire and the grounded grid. The emitter wire electrode is fixed at 10 mm from the channel inlet, whereas the location of the collecting grid is at different distances, G, from the corona wire. The effect of several geometric parameters, including the corona wire diameter, the electrode gap between emitter and collecting grid (G), the collector location, and the distribution of collecting grid wires, on the characteristics of EHD blowers of different heights is investigated. The same modelling values used in the validation simulation are adopted in this numerical investigation, while the geometric parameters of the present EHD air blower configuration and the distribution of collecting grid for each blower height, h, are detailed in **Tables 3** and **4**, respectively.

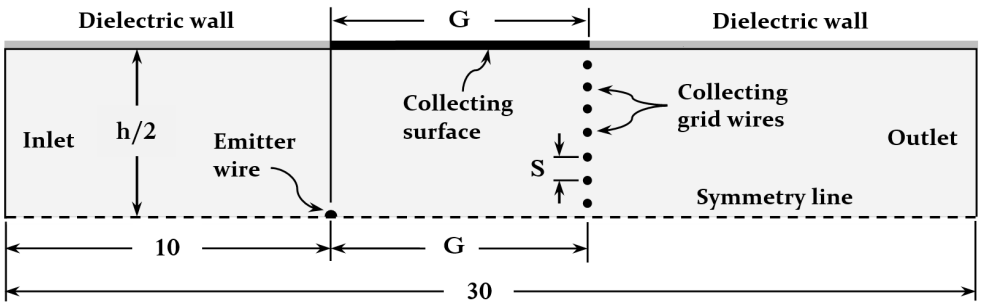

Fig. 6. Half domain of the EHD blower geometry used in the present numerical study. Dimensions in millimetres.

Table 3. Modelling parameter values and ranges of the present numerical configuration.

Modelling parameter	Value
Corona wire diameter, d	50, 100, 150 μm
Blower length, L	30 mm
Blower height, h	9 – 15 mm
Number of collecting grid wires, N	6 – 14 wires
Electrode gap between emitter and collecting grid, G	5 – 10 mm
Horizontal distance between emitter and collecting surface, b	0 – 4 mm

Table 4. Distribution of the collecting grid wires for different blower heights, each with S = 1 mm.

Blower height, h (mm)	Number of grid wires, N	Spacing between grid wires, S (mm)
9	8	1
11	10	1
13	12	1
15	14	1

4.2 Influence of emitter wire diameter

The effect of the emitter wire diameter, d, on the EHD blower performance is first explored by considering three levels of wire diameter with 50, 100 and 150 μm, each modelled for an EHD blower with height of h = 15 mm at a fixed electrode gap of G = 8 mm. **Fig. 7** shows how the corona current and the generated air velocity increase as the diameter of the emitter wire decreases at a given applied voltage, due to the stronger electric field created by the higher tip curvature. This trend can be explained based on the definition of the ion current,

$$I_{\mathrm{c}} = (\mu_{\mathrm{p}} \vec{E} q)\, A_{\mathrm{w}} \tag{8}$$

where A_{w} is the surface area of the corona wire (calculated per wire length). Since both the ion mobility μ_{p} and A_{w} are assumed constant, the ion current changes proportionally to the body force, $\vec{F}$

$$I_{\mathrm{c}} \propto \vec{F} \propto \vec{E} q \tag{9}$$

According to Peek's formula (Eq. 7), the electric field intensity $\vec{E}$ is inversely proportional to the diameter squared of the corona wire. This in turn suggests that the ion current has the following relationship,

$$I_{\mathrm{c}} \propto \vec{E} \propto \frac{1}{d^2} \tag{10}$$

Hence, at a given applied voltage and an electrode gap, when the emitter wire diameter decreases, both the corona current and the electric field intensity increase, enhancing the Coulomb force and the kinetic energy imparted to the airflow.

In all cases, the applied voltage must exceed the critical corona onset voltage before the corona wind is created. In addition, as reported in [**14**], the onset voltage decreases as d decreases, so that the power consumption required to generate a certain corona wind velocity can be reduced by decreasing d. For example, an emitter wire with d = 50 µm requires 2.5 W/m (at a voltage of 5 kV) to generate an air velocity of 0.86 m/s, compared with 3 W/m (at 6 kV) consumed by a wire with d = 100 µm to produce nearly the same air velocity, as can be seen in **Fig. 7(b)**.

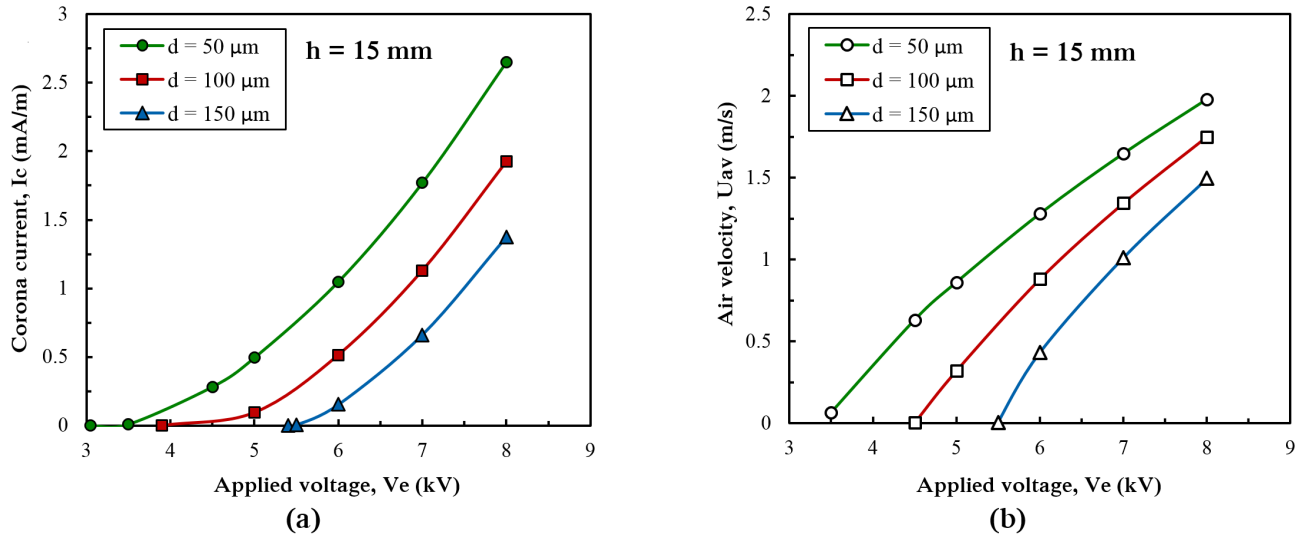

Fig. 7. Effect of emitter wire diameter, d, at G = 8 mm, on (a) corona current, and (b) average air velocity, for a range of applied voltage.

In order to investigate the EHD blower performance for different emitter wire diameters and collecting grid locations, the electro-mechanical efficiency, which is the percentage of electrical power converted into mechanical (kinetic) power, is adopted and given by [**24**, **35**, **36**],

$$\eta = \frac{P_{\text{mech}}}{P_{\text{elec}}} \tag{11}$$

The mechanical power calculated per channel width can be expressed as,

$$P_{\text{mech}} = \frac{1}{2}\,\rho\, h\, U_{\text{av}}^{3} \tag{12}$$

where ρ is the air density (kg/m^3), U_{av} is the average air velocity at the channel outlet (m/s), and h is the channel outlet height (m). The electrical power P_{elec} can be defined by,

$$P_{\text{elec}} = V_{\text{e}}\, I_{\text{c}} \tag{13}$$

where V_{e} is the applied potential (V), and I_{c} is the corona current calculated per the channel width (or corona wire length) (A/m).

Fig. 8 studies the effect of both d and G on the blower performance at an applied voltage of 7 kV and a range of electrode gaps. The figure demonstrates that the blower efficiency, η, with the finer electrode is the highest for the range of electrode gaps, compared with using thicker wires, which reveal lower performance with a drop in the efficiency as the gap increases. This indicates that the distribution of the stronger electric field intensity created by the finest wire has greater impact on the ionic wind production, regardless of the increase in the created ion current. It is important to state that the very low values of the electro-mechanical efficiency achieved in the present configuration due to the corona discharge lay within the expected range ($\ll 1$) that was previously found and demonstrated [**36**, **37**].

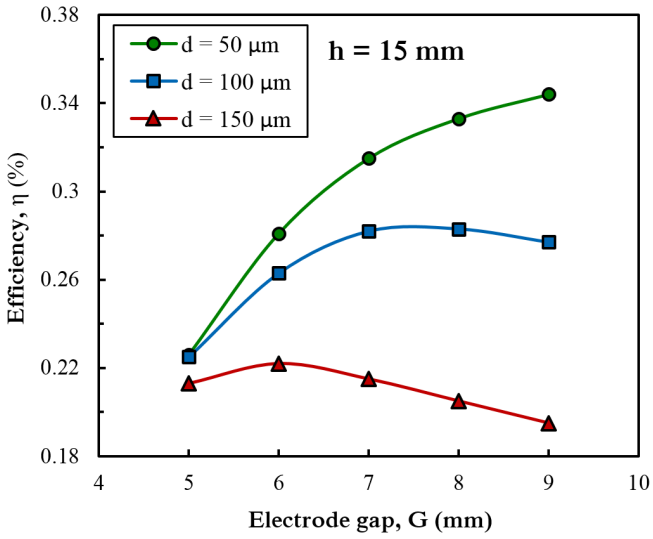

Fig. 8. Effect of electrode gap, G, on blower efficiency for different emitter wires modelled at 7 kV for blower of h = 15 mm.

Fig. 9 compares the efficiency and the ion current created by two different wires with 50 µm and 100 µm diameters at different applied voltages. It shows that the corona current created by both wires declines as the electrode gap increases, resulting in a significant growth in the blower efficiency. However, although the current created by the thicker wire with d = 100 µm at 8 kV is higher than that created by the finer wire with d = 50 µm at lower potential (7 kV), the latter electrode reveals higher efficiency over the range of electrode gaps. This is mainly due to the stronger electric field intensity and the effective distribution of its lines along the collecting surface and the grid wires, which are responsible for imparting higher kinetic energy to the airflow in the outlet direction. In contrast, the lower electric field intensity created by the thicker wire is highly affected by the closer area at undesirable directions of the collecting

surfaces, leading to a drop in the efficiency. It was noticed, for example, that using the finer wire at G = 8 mm reduces the power consumption and the required voltage by 3 W/m (20% gain) and 1 kV, respectively, whereas the ionic wind velocity is decreased with only 0.1 m/s (approximately 6% drop), compared to the case of using the thicker wire with the same electrode gap. From a design perspective, using a finer wire electrode can decrease both the power consumption and the applied potential required to generate a certain air velocity, improving the EHD blower performance. Therefore, the finest emitter wire with 50 μm diameter will be adopted for the remainder of this study.

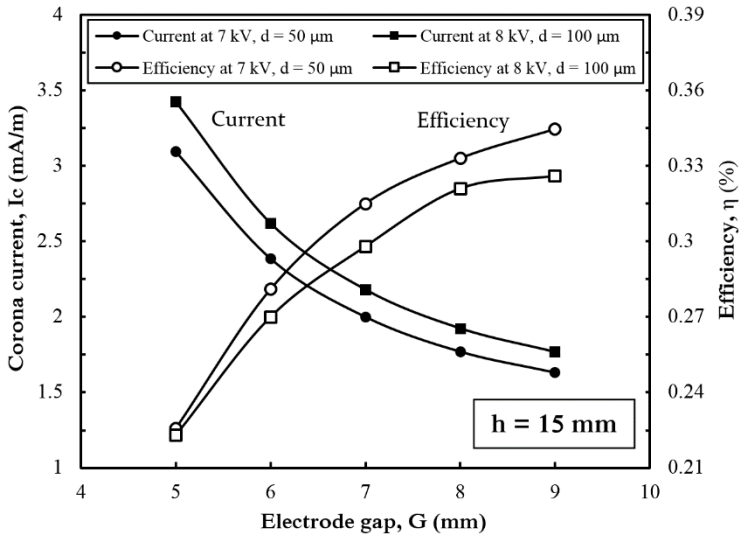

Fig. 9. Comparisons of the ion current (left axis) and the efficiency (right axis) created by two different wires at different applied voltages, for h = 15 mm and a range of electrode gaps.

4.3 Influence of electrode gap

This section discusses the influence of the distance, G, between the emitter wire and the collecting grid electrodes on the EHD power and airflow velocity, which will be presented for the blower of 15 mm height as a case study. **Fig. 10** shows plots of the square root of the corona current (calculated based on wire length) and the generated air velocity as a function of the applied voltage for different electrode gaps (G = 5 to 10 mm). The general trends indicate that both corona current and air velocity increase with increasing applied voltage or decreasing electrode gap. Indeed, the increase in the applied voltage at a given electrode gap, or the decrease in the latter at a given applied voltage, increases the electric field and the resulting Coulomb force, according to Poisson's equation (Eq. 1). This in turn increases the kinetic energy imparted to the electrons (moving towards the positive wire electrode) and to the positive charged ions (moving towards the grounded electrode), leading to a greater corona current and a higher ionic wind generation. The voltage-current characteristics shown in **Fig. 10a** demonstrate a linear relationship between the applied potential and the square root of corona current in the present numerical configuration, confirming previous findings presented by Robinson [**11**] and others [**38**, **39**].

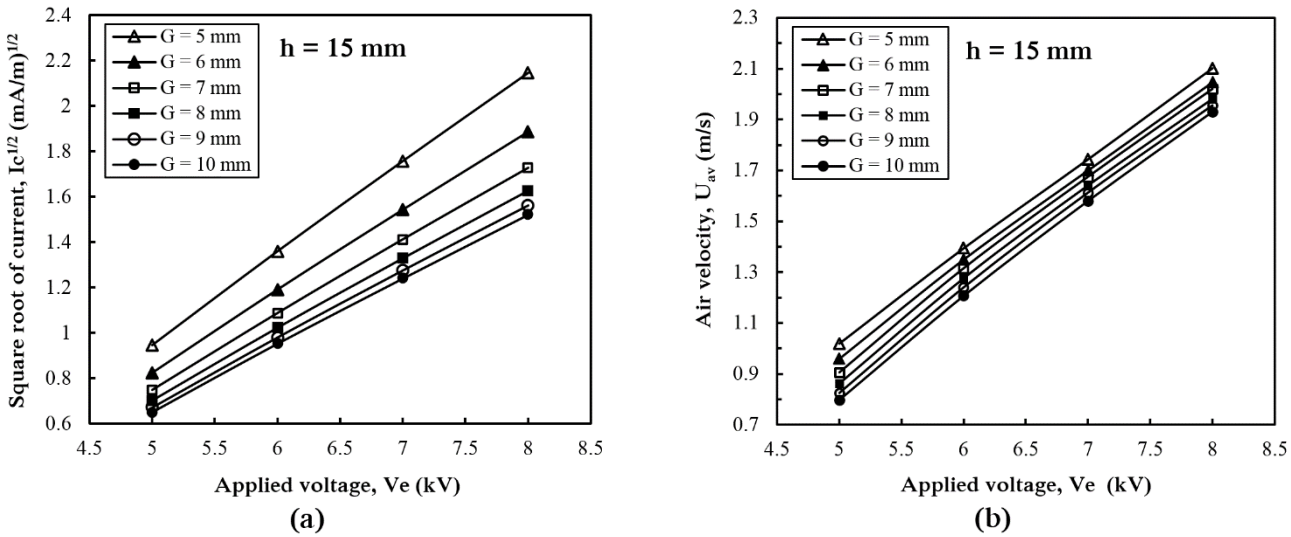

Fig. 10. Effect of electrode gap, G, and applied voltage on (a) corona current, and (b) average air velocity at the channel outlet.

Fig. 11 illustrates how the efficiency increases as the applied voltage and the electrode gap increase, reaching the peak level at their higher values. However, at smaller electrode gaps (G = 5 and 6 mm), the blower efficiency tends to remain constant or decline slightly with increasing applied voltage. This can be attributed to the impact of the electric field distribution along the grounded grid wires, and also due to the effect of the collecting surface length at the channel wall, which increases with the electrode gap G. Indeed, when the applied voltage increases at small electrode gaps, the electric field intensity becomes stronger and highly affected by the upper grid wires and the short grounded surface located above the corona electrode, which is not the desired flow direction. Therefore, the concentration of the electric field lines and the body force vectors towards the collecting surface will increase, decreasing relatively the impact of the horizontal components of the Coulomb force, which is responsible for moving the ionic wind towards the channel outlet, and leading to lower efficiency. Moreover, the same behaviour occurs for the higher electrode gaps (G = 9 and 10 mm) at low applied voltage, where the electric field lines are highly affected by the collecting surface, which is closer to the corona wire than the grounded grid.

In contrast, at higher potential and electric field intensity, the increase in the electrode gap and the collecting surface length improves the distribution of the electric field lines along the grounded surface and increases the drifting angle between the emitter and the grid electrodes, enhancing the ions charge drifted in the horizontal path. Further explanation can be obtained from **Fig. 12**, which shows two distributions of the space charge density with the body force arrows generated at 8 kV for electrode gaps of G = 5 and 8 mm. It is found that although the power consumed by the blower at G = 5 mm is approximately 36.8 W/m, compared to 21.2 W/m at G = 8 mm (with 42.4% drop), the difference in the average velocity is no more than 0.11 m/s (about 5% decrease), showing the significant effect of the grounded surfaces location on the EHD blower efficiency.

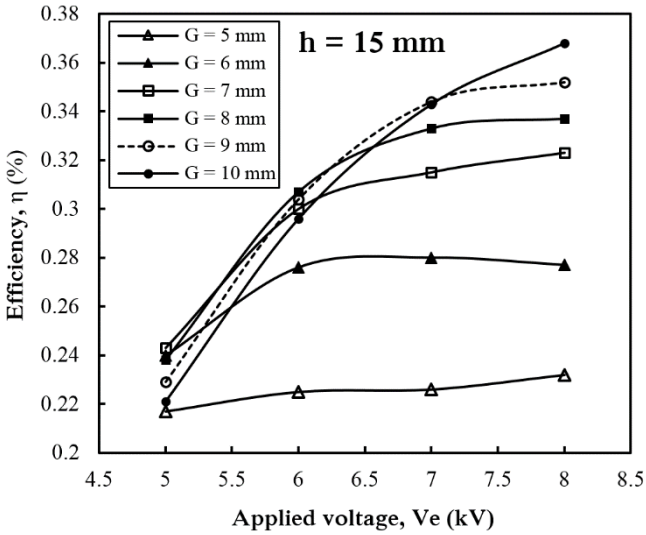

Fig. 11. Effect of electrode gap, G, on blower efficiency at constant applied voltages.

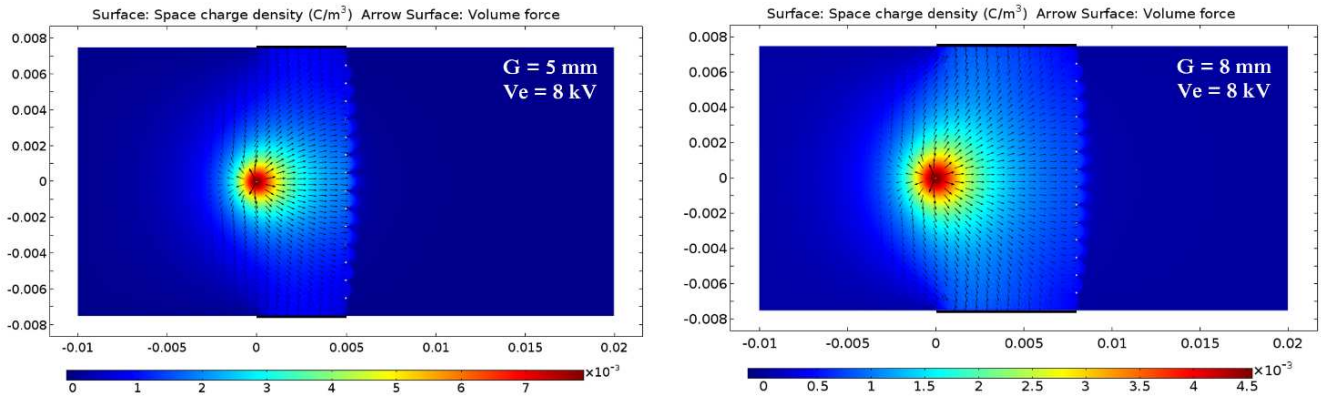

Fig. 12. Distributions of the space charge density with the body force arrows generated at 8 kV for h = 15 mm and electrode gaps of G = 5 and 8 mm.

4.4 Optimization of electrode gap

The optimization of the collecting grid location from the emitter electrode, defined by electrode gap, G, for each blower height is now explored by fixing the operating power at constant levels. The input power was varied from 2.5 to 15 W/m, which corresponds to an overall range of applied voltage from 3.97 to 7.6 kV required for all ranges of electrode gaps and blower heights. **Fig.13** illustrates the influence of the electrode gap on the efficiency of different blowers for a range of input power. It can be observed that the efficiency increases as the input power increases at each electrode gap of all blowers, which is due to the stronger electric field created by the higher potential. Furthermore, the difference in the blower efficiency values due to changing the electrode gap fluctuates from blower to another, depending on the height and the level of operating power. However, the trends show that the efficiency of each blower reaches its maximum value at certain location for all input powers, revealing the unfavorable impact of increasing the electrode gap beyond this point. Indeed, with further increases in the electrode gap, the electric field lines become highly affected by the collecting surface, which will be closer to the

corona wire than the grounded grid, leading to a drop in the efficiency. Therefore, these locations (identified in **Fig. 13** by dashed lines), where the highest blower efficiency is achieved, can be considered the optimal electrode gaps for the present configuration, and are listed in **Table 5**.

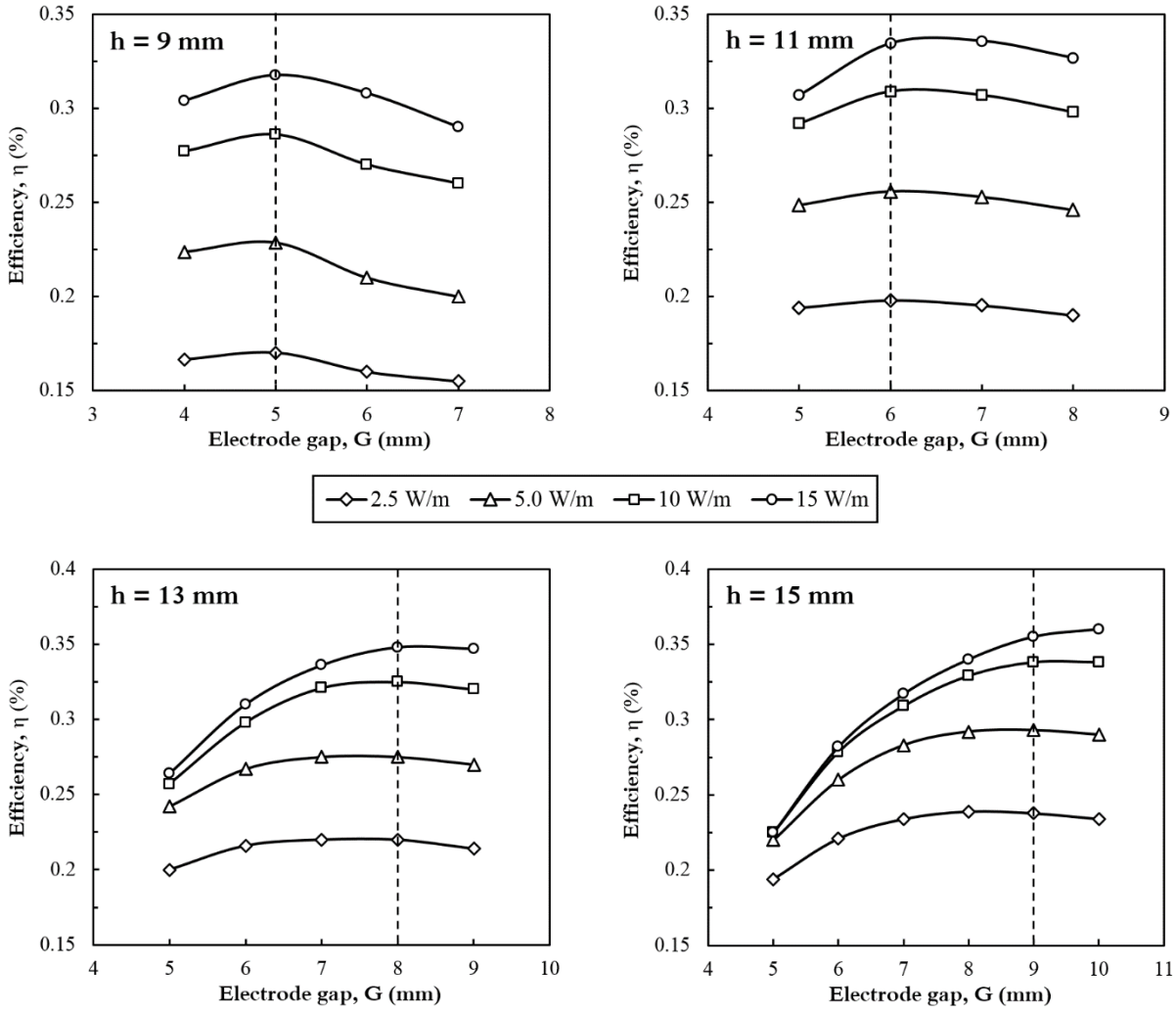

Fig. 13. Effect of electrode gap, G, on efficiency of different blowers at fixed input powers. (Dashed lines indicate the optimal electrode gaps)

Table 5. Optimal locations (defined by electrode gap, G) of the collecting grid from the emitter wire for different EHD blowers.

Blower height, h (mm)	Electrode gap, G (mm)	Collector length (= G), (mm)	Number of grid wires, N
9	5	5	8
11	6	6	10
13	8	8	12
15	9	9	14

4.5 Optimization of collecting surface location

The influence of the collecting surface location at the blower walls on the EHD blower performance is now discussed. The collecting grid was fixed at the optimal electrode gap of each blower, while the

horizontal distance, b, between the emitter wire and the edge of the collector electrode was changed from b = 0 (the original position) in 1 mm steps, decreasing the collector length to a distance of $(G - b)$, as shown in **Fig. 14**. In order to predict the optimal location of the grounded surface of each blower and its impact on the EHD blower performance, the investigation is performed based on the blower efficiency by fixing the applied potential (calculated only for the blower of 15 mm height) and the input power, and the results are compared to those of a blower without collecting surfaces (NCS) at its walls.

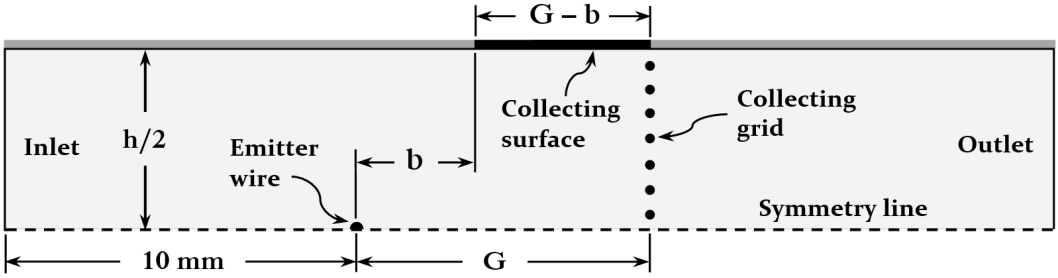

Fig. 14. The collecting surface location based on the horizontal distance, b, from the emitter wire electrode.

Fig. 15 shows the collector location as a function of the EHD blower efficiency and the resulting air velocity for a range of applied voltages. It can be seen that the ionic wind velocity grows significantly in the presence of the collecting surface at b = 0, compared to the case of no collector, before it tends to decrease as the distance b increases, whereas their efficiency are nearly at the same level. This is caused by the higher corona current created between the electrodes due to increasing the collector area, compared to that created just by the grounded grid, resulting in higher ionic wind production. In addition, the trends of the efficiency bars show an obvious increase as the collecting surface moves apart from the emitter wire, reaching peak values at nearly b = 3 mm. Despite the highest air production obtained at b = 0, which agrees with previous experimental findings presented in [**23**], moving the collector to the location of b = 3 mm shows that the maximum decrease in the velocity (at 8 kV for instance) is approximately 10%, while a significant reduction in the power consumption of 43.5% is achieved. Indeed, moving the collecting surface with the flow direction towards the channel outlet can enhance the electric field distribution on the collecting surfaces and strengthen the horizontal component of the Coulomb force, decreasing the corona current created due to the narrow gaps, and resulting in better EHD efficiency.

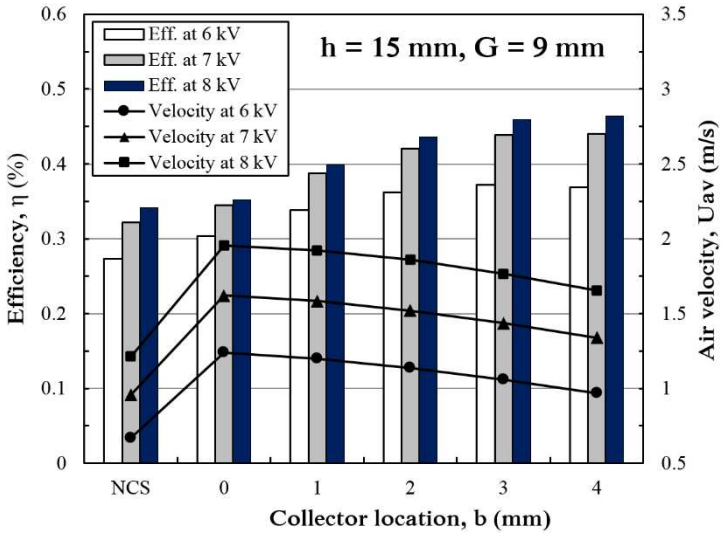

Fig. 15. Effect of collector location (defined by b) on blower efficiency (left axis) and air velocity (right axis), for a range of applied voltage.

For the case of fixing the input power, **Fig. 16** illustrates the impact of the collector location of different blowers on the outlet air velocity and the applied voltage that corresponds to each level of input power. It also indicates that the presence of the collecting surface at $b = 0$ can reduce the required voltage by approximately 3 kV at 15 W/m for $h = 15$ mm, as an example, and produce nearly the same air velocity of that generated by a blower with just a collecting grid. The general trends show that both the ionic wind velocity and the corona voltage required to preserve the input power at a constant level increase with distance b. These observations are similar to the experimental observations of a flow in an open space reported in [**20**]. However, the values of air velocity produced by each blower tend to decrease or increase very slightly after certain locations, for the two levels of operating power.

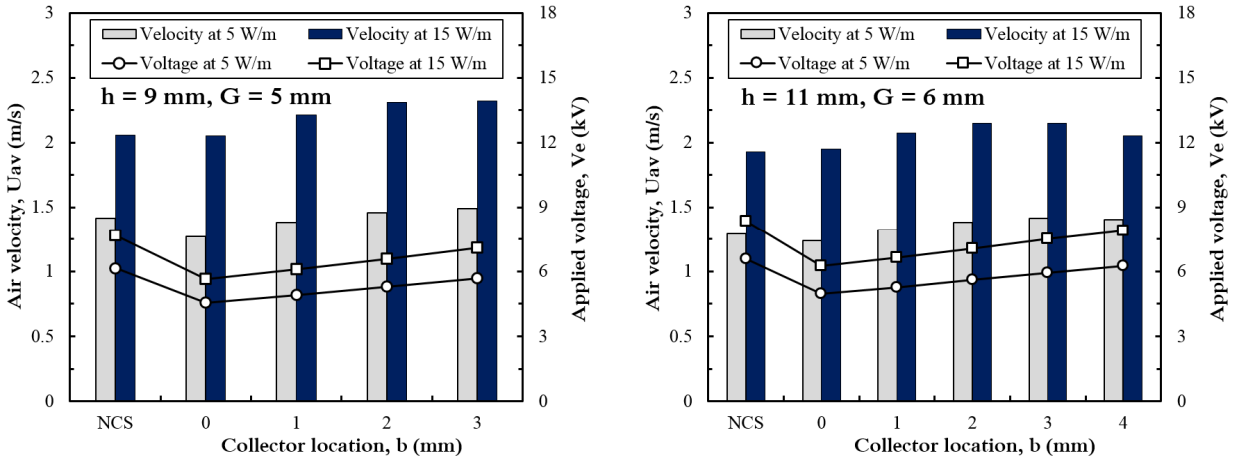

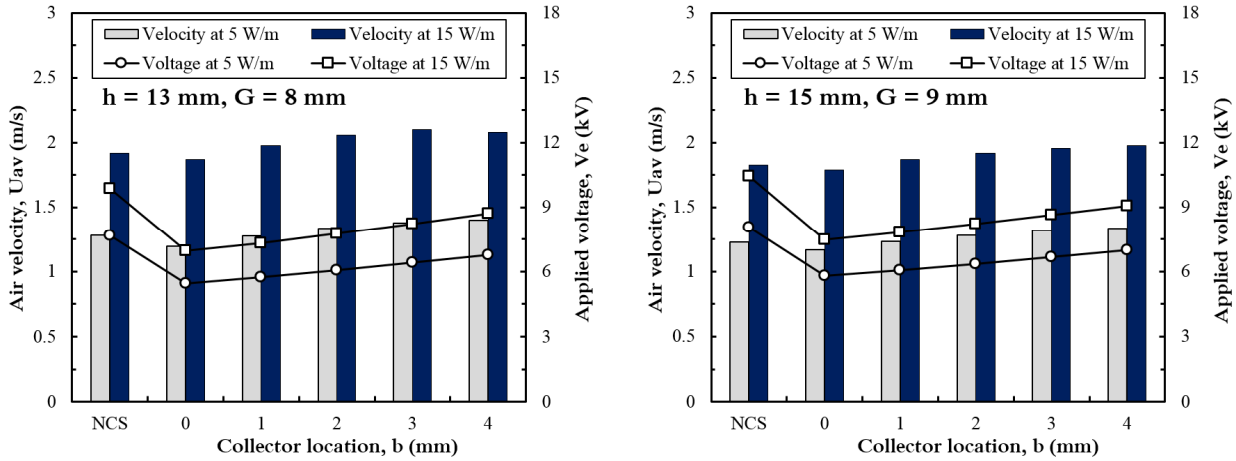

Fig. 16. Effect of collector location of different EHD blowers on the air velocity (left axis) and the applied voltage (right axis), at two levels of fixed input power.

In order to reduce the level of the applied voltage and determine the most effective location of the collecting surface for each blower height, the percentage increases of both the average velocity and the applied potential were calculated for different collector locations (defined by b) at two levels of input power, as illustrated in **Fig. 17**. It is clear that the percentage increase in the air velocity at the first step (b = 1 mm), over that generated at the location of b = 0, is higher than that of the required applied potential for all blower heights. However, the augmentation in the velocity tends to decrease with increasing b, compared to that of the potential, and (the latter) reaches its peak level at certain locations before it tends to decrease. It is found that when the increase in the potential reaches its peak, the increase in the air production accounts for approximately 50% or higher than that of in the applied voltage, and all increases in the voltage beyond these gaps lead to a drop (shown with red bars) or relatively very slight improvements in the air velocity. These locations, which are indicated by arrows in the figure, can be considered as the optimal and the most effective gaps at constant input power, as detailed in **Table 6**.

Based on these optimal locations, the maximum enhancements achieved in the average outlet velocity are between 9% and 15%, depending on blower thickness, compared to those obtained at b = 0, using the same operating power.

Table 6. Optimal collector locations from the emitter wire for different EHD blowers, determined based on effective increase in the applied voltages at fixed operating powers.

Blower height, h (mm)	Optimal collector location, b (mm)	Electrode gap, G (mm)	Collector length, CL (= G – b) (mm)	Number of grid wires, N
9	2	5	3	8
11	2	6	4	10
13	3	8	5	12
15	3	9	6	14

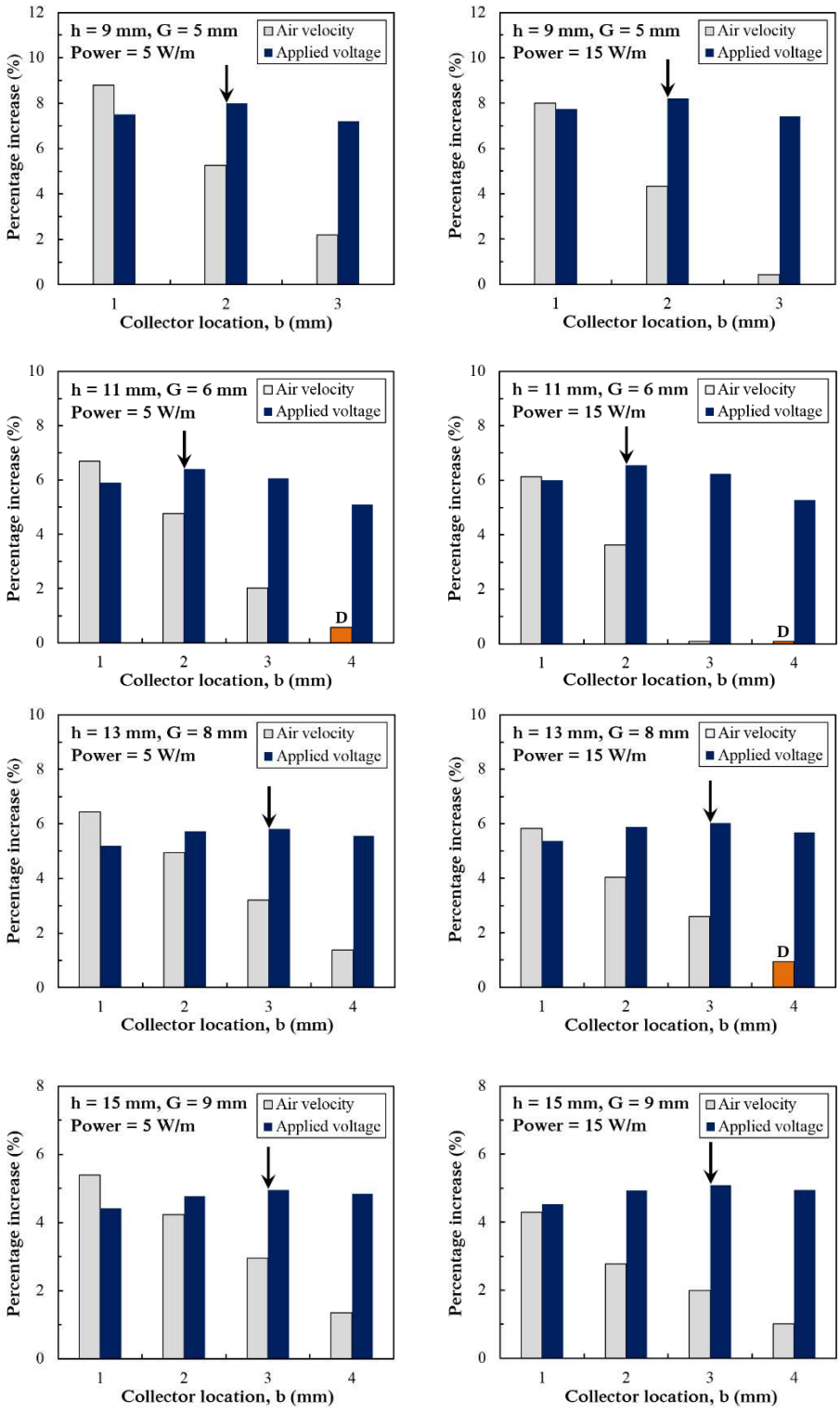

Fig. 17. Collector location as a function of the percentage increase (each calculated over that of the former location, b) in both air velocity and the applied potential for different blowers at fixed input powers (5W/m for left column and 15 W/m for right column). Arrows indicate the optimal collector locations, and red bars refer to a decrease (D).

4.6 Effect of collecting grid on blower performance

In order to explore the advantage of using the grid wires as further collecting surfaces for the blower performance, a comparison based on the required operating voltage and the blower length (or size) was established. Two blower heights with h = 9 and 15 mm were selected and modeled with no collecting grid

(named as the NG case) at a fixed power of 15 W/m, and their results were compared to those obtained by equivalent blowers with a collecting grid (named as the WG case).

The first comparison was performed based on the required operating voltage by fixing the collector length at (CL $= G - b$), in order to ensure the same blower length in both compared cases. **Fig. 18** shows that the NG case requires higher applied voltage to fix the operating power at a constant level at all given collector locations of both presented blowers, with an increase reaches to approximately 12% at the optimal locations of both blowers, compared to the WG case. In contrast, the velocity trends reveal obvious reductions at all collector locations of both blowers, which appear higher for the thinner blower due to its shorter collector length. This clearly reflects the important role of using the collecting grid in increasing the collecting surface area and thereby reducing the level of operating voltage, and at the same time improving the electric field distribution in the desirable direction with higher kinetic energy imparted to the flow towards the blower outlet.

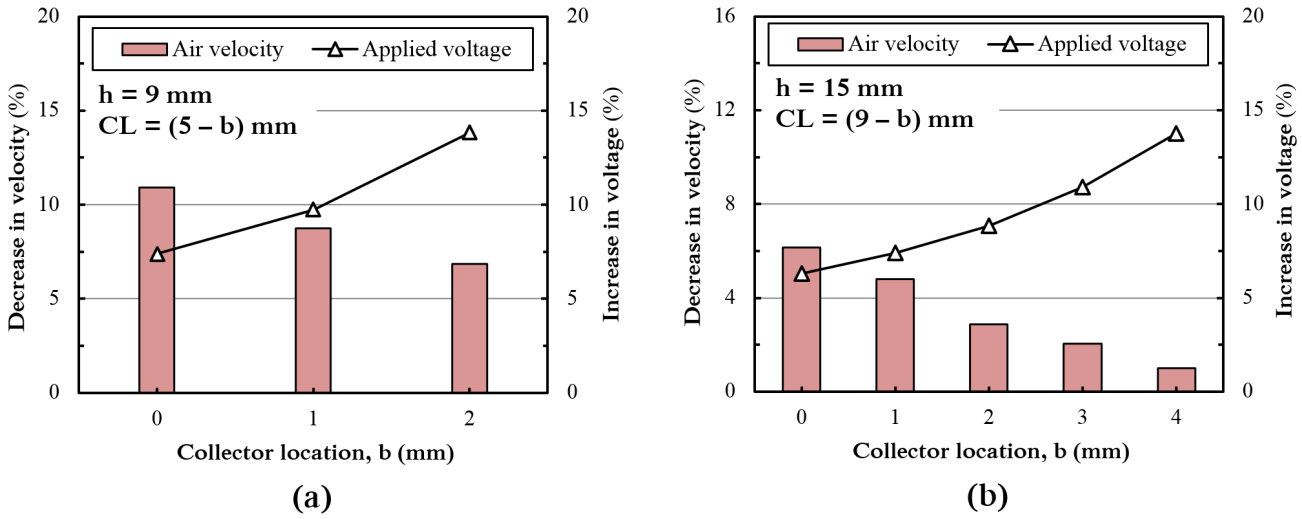

Fig. 18. Percentage decrease in air velocity and increase in applied voltage for blowers without collecting grid (NG), compared to those with a grid (WG), modelled with fixed collector length at (G – b) and different collector locations, for blower heights of (a) h = 9 mm, and (b) h = 15 mm.

The blower length was considered in the second comparison, which can be defined as the actual distance between the corona wire and the far end of collector electrode. Although the numerical domain length of both cases used in the presented comparison is 30 mm, the percentage increase in the blower length was calculated by assuming that the blower lengths of WG case are 6 mm (for h = 9 mm) and 10 mm (for h = 15 mm), which are the actual minimum lengths that can be used in the practical implementation.

For the NG case, the collector lengths were fixed at 5 and 9 mm for blowers of h = 9 and 15 mm, respectively, regardless the collector locations from the emitter wire, whereas their results were compared to those obtained by optimized blowers of WG case but with collector lengths equal to ($G - b$). This in

turn leads to an increase in the blower length of NG case as the collector moves away from the emitter wire, compared to that of WG case, which is restricted by the wire-to-grid electrode gap, G.

Fig. 19 shows that although the collecting surface lengths of the blowers for NG case remain constant at all locations, the use of collecting grid still offers lower operating voltage required for both blowers at all collector locations. This increase is accompanied by a drop in the air velocity (shown by red bars) and an increase in the blower length before modest enhancements in the velocity (green bars) are achieved as the collectors move towards the blower outlet but with higher operating voltage and larger blower size. These observations also indicate that using the grid as an additional collecting surface electrode has significantly positive impacts on the blower performance with higher flow production and lower size and operating voltage, meeting the design and thermal management requirements.

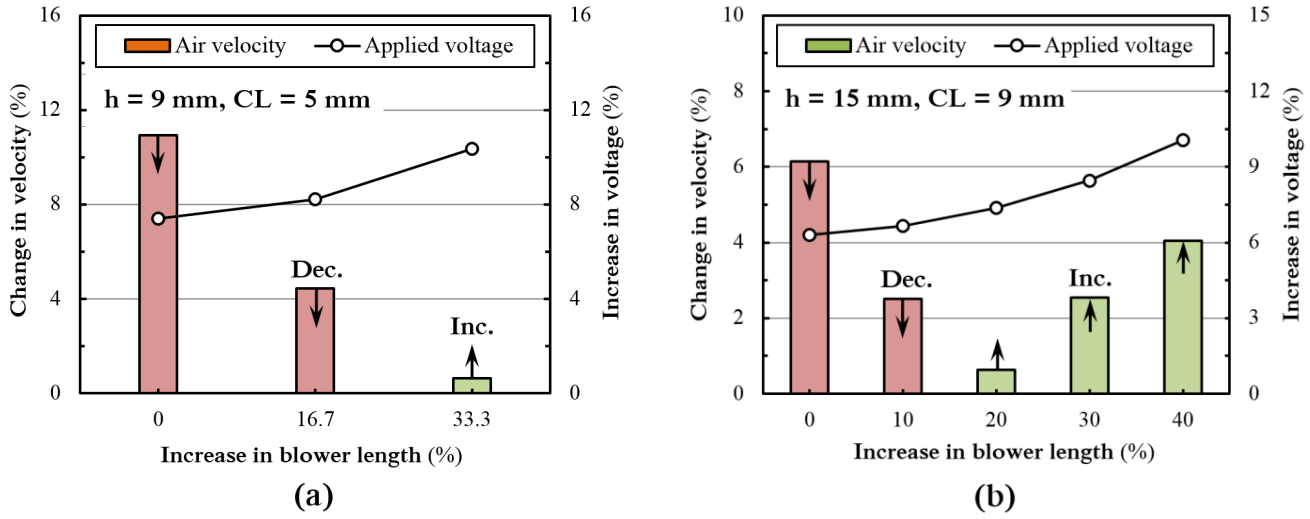

Fig. 19. Percentage change in blower length, air velocity, and applied voltage of blowers without collecting grid (NG), compared to those with a grid (WG), for blower heights of (a) h = 9 mm, and (b) h = 15 mm.

4.7 Effect of collecting grid density

The final section illustrates the effect of the collecting grid density on the efficiency of each optimized blower by considering different levels of grid density, defined by the number of wires (N) and the spacing of the gaps separating two successive wires (S), as described in **Table 7**. The locations of both the grid and the collecting surface of each blower are fixed at their optimal predicted gaps from the emitter wire. The investigation is performed at two levels of constant applied voltage, which correspond to those required to fix the power at 5 and 15 W/m, respectively, and used in each case of optimized blower. The case that without collecting grid (N = 0) is included to reflect its impact on the blower performance.

Table 7. Description of the collecting grid densities used in different blowers based on the number of grid wires (N) and distances between two successive wires (S). Bold figures refer to the initial (finest) grid density assigned for each blower height.

Blower height, h (mm)	Grid density	GN0	GN6	GN8	GN10	GN12	GN14
15	**Number of wires, N**	0	6	8	10	12	**14**
	Spacing, S (mm)	–	2.5	2	1.5	1.25	**1**
13	**N**	0	6	8	10	**12**	–
	S	–	2	1.5	1.25	**1**	–
11	**N**	0	6	8	**10**	–	–
	S	–	1.8	1.25	**1**	–	–
9	**N**	0	6	**8**	–	–	–
	S	–	1.5	**1**	–	–	–

Fig. 20 shows air velocity and power consumption as functions of the number of collecting grid wires for different blower heights modelled at a constant voltage required to fix the power at 15 W/m for each blower. It reflects that decreasing the grid density reduces the power consumed by each blower, whereas the velocity trends show different behaviour depending on the number of grid wires of each blower. In addition, both the velocity and power consumption values obtained by using any grid density of each blower are higher than those of the no-grid case, GN0 (N = 0).

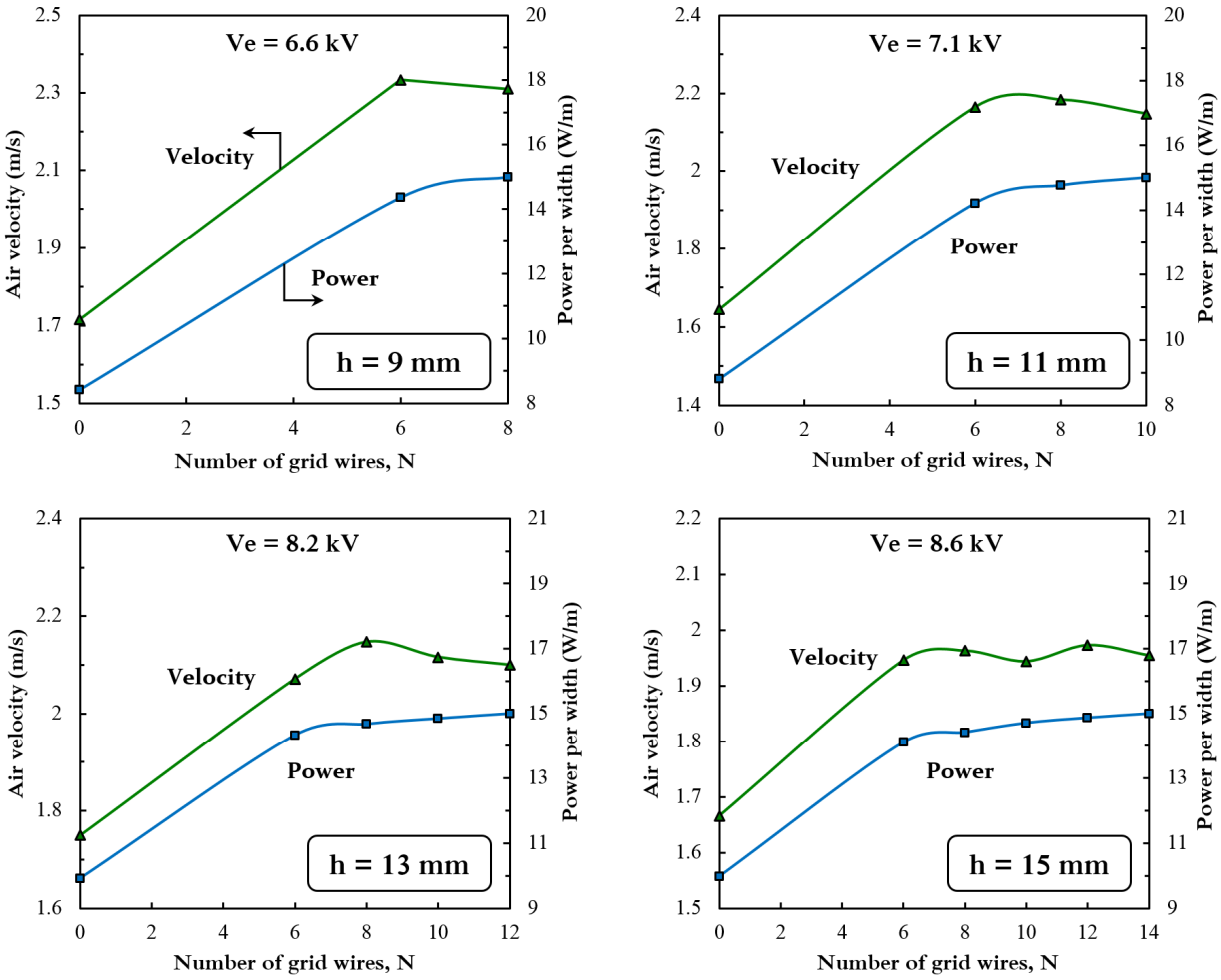

Fig. 20. Effect of the grid density on average air velocity (left axis) and power consumption (right axis) for different blowers, each operated at a constant applied voltage required to fix the power at 15 W/m.

In order to reflect the impact of the grid density on the blower performance, the electro-mechanical efficiency of each blower was calculated at two levels of applied voltage, as shown in **Fig. 21**. It illustrates that the efficiency of each blower at the two applied voltages reaches its highest values with a certain grid density before it tends to fall as the grid becomes denser. In all cases, using the grid as a further collecting electrodes reveals higher blower efficiency over the case of a blower without grid. The figures of the highest efficiency show that using a coarse collecting grid with 6 and 8 wires for the thin and thick blowers, respectively, is effective and offers better blower performance, which follows previous recommendations presented in [**24**, **26**]. This behaviour can be attributed to the balance occurring between the decrease in the grounded area and the increase in the spacing of flow paths through the grid. Indeed, the slight reduction in both the ion current and the impact of the body force due to decreasing the number of collecting wires can be compensated by a decrease in the pressure losses caused by the narrow flow paths through the grid wires.

Based on these predicted results and from a design perspective, using a coarse collecting grid offers better flow velocity and reduces the power consumption, the pressure losses and additionally the manufacturing complexity.

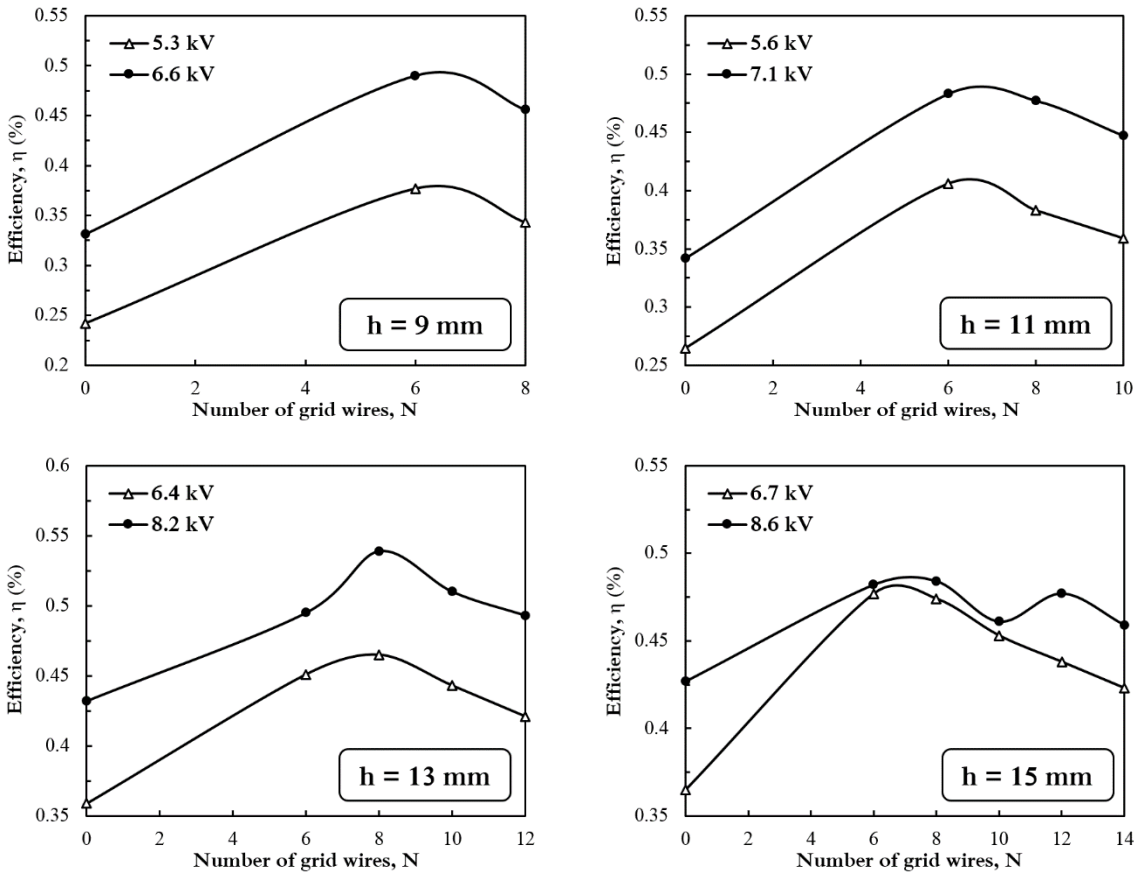

Fig. 21. Grid density as a function of blower efficiency calculated for different blowers at two levels of applied potential that required to fix the powers at 5 and 15 W/m in each blower.

5. Conclusions

An accurate numerical approach has been performed to solve the coupled electric field, charge transport and airflow equations for EHD air pumps. This has been used to carry out a comprehensive parametric study into the effect of the corona wire diameter, collecting electrodes gaps and collecting grid distribution on the efficiency of the EHD wire-to-grid blowers.

It is found that using a fine emitter wire is more efficient than a thicker one as it decreases the power consumption and the applied potential required to generate a certain air velocity. The numerical results reveal that the presence of the grid as a further collector increases the blower performance, with higher flow production, lower operating voltage and reduced blower size. Results also demonstrate that the grounded electrodes' locations highly affect the electric field distribution and the blower efficiency, and the latter can be enhanced by increasing the electrode gap of both collectors from the emitter wire, due to the increase in both the drifting angle of the ions charge and the kinetic energy imparted to the flow towards the blower outlet.

The optimal electrode gap of both the grid and the collecting surface for each blower can be determined based on the effective increase in the applied voltage by fixing the operating power. The optimal locations of both collectors show that the average outlet velocity (or the blower efficiency) is enhanced with maximum increases in the range from 9% to 15%, depending on blower thickness, compared to that obtained with inefficient collector locations using the same operating power.

However, further work is still needed to investigate more geometrical parameters related to the wire-to-grid channel configuration such as the collecting wires diameters, the grid distributions in an inclined and curved arrangements as well as the electrode spacing.

Acknowledgements

Funding support from the Higher Committee for Education Development in Iraq (HCED Ref. No. D-11-3102) is gratefully acknowledged.

References

1. Sahin, B. and A. Demir, *Performance analysis of a heat exchanger having perforated square fins.* Applied Thermal Engineering, 2008. **28**(5): p. 621-632.
2. Zimmermann, S., I. Meijer, M.K. Tiwari, S. Paredes, B. Michel, and D. Poulikakos, *Aquasar: A hot water cooled data center with direct energy reuse.* Energy, 2012. **43**(1): p. 237-245.
3. Hopton, P. and J. Summers. *Enclosed liquid natural convection as a means of transferring heat from microelectronics to cold plates*. in *Semiconductor Thermal Measurement and Management Symposium (SEMI-THERM), 2013 29th Annual IEEE*. 2013. IEEE.
4. Patterson, M.K. *The effect of data center temperature on energy efficiency*. in *Thermal and Thermomechanical Phenomena in Electronic Systems, 2008. ITHERM 2008. 11th Intersociety Conference on*. 2008. IEEE.
5. Breen, T.J., E.J. Walsh, J. Punch, A.J. Shah, C.E. Bash, N. Kumari, et al., *From Chip to Cooling Tower Data Center Modeling: Chip Leakage Power and Its Impact on Cooling Infrastructure Energy Efficiency.* Journal of Electronic Packaging, 2012. **134**(4): p. 041009.
6. Jewell-Larsen, N., H. Ran, Y. Zhang, M. Schwiebert, K.H. Tessera, and A. Mamishev. *Electrohydrodynamic (EHD) cooled laptop*. in *Semiconductor Thermal Measurement and Management Symposium, 2009. SEMI-THERM 2009. 25th Annual IEEE*. 2009. IEEE.
7. Wang, H.-C., N.E. Jewell-Larsen, and A.V. Mamishev, *Thermal management of microelectronics with electrostatic fluid accelerators.* Applied Thermal Engineering, 2013. **51**(1): p. 190-211.

8. Jewell-Larsen, N., C. Hsu, I. Krichtafovitch, S. Montgomery, J. Dibene, and A.V. Mamishev, *CFD analysis of electrostatic fluid accelerators for forced convection cooling.* Dielectrics and Electrical Insulation, IEEE Transactions on, 2008. **15**(6): p. 1745-1753.
9. Fylladitakis, E.D., M.P. Theodoridis, and A.X. Moronis, *Review on the history, research, and applications of electrohydrodynamics.* Plasma Science, IEEE Transactions on, 2014. **42**(2): p. 358-375.
10. Stuetzer, O.M., *Ion drag pressure generation.* Journal of Applied Physics, 1959. **30**(7): p. 984-994.
11. Robinson, M., *Movement of air in the electric wind of the corona discharge.* American Institute of Electrical Engineers, Part I: Communication and Electronics, Transactions of the, 1961. **80**(2): p. 143-150.
12. Marco, S. and H. Velkoff, *Effect of electrostatic fields on free-convection heat transfer from flat plates.* ASME Paper No. 63-HT-9, 1963.
13. Kulacki, F., *Electrohydrodynamic enhancement of convective heat and mass transfer.* Advances in transport processes, 1982. **2**: p. 105-147.
14. Franke, M. and L. Hogue, *Electrostatic cooling of a horizontal cylinder.* Journal of heat transfer, 1991. **113**(3): p. 544-548.
15. Owsenek, B. and J. Seyed-Yagoobi, *Theoretical and experimental study of electrohydrodynamic heat transfer enhancement through wire-plate corona discharge.* Journal of Heat Transfer, 1997. **119**(3): p. 604-610.
16. Ohadi, M., J. Darabi, and B. Roget, *Electrode design, fabrication, and materials science for EHD-enhanced heat and mass transport.* Annual Review of Heat Transfer, 2000. **11**(11).
17. Shooshtari, A., M. Ohadi, and F.H. França. *Experimental and numerical analysis of electrohydrodynamic enhancement of heat transfer in air laminar channel flow*. in *Semiconductor Thermal Measurement and Management Symposium, 2003. Ninteenth Annual IEEE*. 2003. IEEE.
18. Go, D.B., S.V. Garimella, and T.S. Fisher. *Numerical simulation of microscale ionic wind for local cooling enhancement*. in *Thermal and Thermomechanical Phenomena in Electronics Systems, 2006. ITHERM'06. The Tenth Intersociety Conference on*. 2006. IEEE.
19. Go, D.B., S.V. Garimella, T.S. Fisher, and R.K. Mongia, *Ionic winds for locally enhanced cooling.* Journal of Applied Physics, 2007. **102**(5): p. 053302.
20. Go, D.B., R.A. Maturana, T.S. Fisher, and S.V. Garimella, *Enhancement of external forced convection by ionic wind.* International Journal of Heat and Mass Transfer, 2008. **51**(25): p. 6047-6053.
21. Go, D.B., R. Maturana, R.K. Mongia, S.V. Garimella, and T.S. Fisher. *Ionic Winds for Enhanced Cooling in Portable Platforms*. in *Electronics Packaging Technology Conference, 2008. EPTC 2008. 10th*. 2008. IEEE.
22. Kalman, H. and E. Sher, *Enhancement of heat transfer by means of a corona wind created by a wire electrode and confined wings assembly.* Applied Thermal Engineering, 2001. **21**(3): p. 265-282.
23. Rashkovan, A., E. Sher, and H. Kalman, *Experimental optimization of an electric blower by corona wind.* Applied Thermal Engineering, 2002. **22**(14): p. 1587-1599.
24. Moreau, E. and G. Touchard, *Enhancing the mechanical efficiency of electric wind in corona discharges.* Journal of Electrostatics, 2008. **66**(1): p. 39-44.
25. Tsubone, H., G. Harvel, K. Urashima, K. Akashi, and J. Chang, *Performance Characteristics of Partially Covered Wire-Parallel Plate Electrodes Type Electrohydrodynamic Gas Pumps.* International Journal of Plasma Environmental Science and Technology, 2013. **7**(1): p. 51-58.
26. Fylladitakis, E.D., A.X. Moronis, and K. Kiousis, *Design of a Prototype EHD Air Pump for Electronic Chip Cooling Applications.* Plasma Science and Technology, 2014. **16**(5): p. 491.
27. Jewell-Larsen, N.E., S.V. Karpov, I.A. Krichtafovitch, V. Jayanty, C.-P. Hsu, and A.V. Mamishev. *Modeling of corona-induced electrohydrodynamic flow with COMSOL multiphysics*. in *Proc. ESA Annual Meeting on Electrostatics, Paper E*. 2008.
28. Mahmoudi, S.R., K. Adamiak, P. Castle, and M. Ashjaee, *The effect of corona discharge on free convection heat transfer from a horizontal cylinder.* Experimental Thermal and Fluid Science, 2010. **34**(5): p. 528-537.
29. Jewell-Larsen, N.E., G.G. Joseph, and K.A. Honer. *Scaling laws for electrohydrodynamic air movers*. in *ASME/JSME 2011 8th Thermal Engineering Joint Conference*. 2011. American Society of Mechanical Engineers.
30. Karpov, S. and I. Krichtafovitch. *Electrohydrodynamic flow modeling using FEMLAB*. in *Excerpt from the Proceedings of the COMSOL Multiphysics User's Conference 2005 Boston*. 2005.
31. Feng, J.Q., *Application of Galerkin finite-element method with Newton iterations in computing steady-state solutions of unipolar charge currents in corona devices.* Journal of Computational Physics, 1999. **151**(2): p. 969-989.
32. Peek, F.W., *Dielectric phenomena in high voltage engineering*. 1920: McGraw-Hill Book Company, Incorporated.
33. Kaptsov, N., *Elektricheskie yavleniya v gazakh i vakuume.* Moscow, OGIZ, 1947.
34. Roth, J.R., *Industrial Plasma Engineering: Volume 2-Applications to Nonthermal Plasma Processing*. Vol. 2. 2001: CRC press.
35. Moreau, E., L. Léger, and G. Touchard, *Effect of a DC surface-corona discharge on a flat plate boundary layer for air flow velocity up to 25m/s.* Journal of electrostatics, 2006. **64**(3): p. 215-225.
36. Moreau, E., *Airflow control by non-thermal plasma actuators.* Journal of Physics D: Applied Physics, 2007. **40**(3): p. 605.
37. Sigmond, R. and I. Lågstad, *Mass and species transport in corona discharges.* High Temp. Chem. Processes, 1993. **2**(4): p. 5.
38. Kibler, K. and H. Carter Jr, *Electrocooling in gases.* Journal of Applied Physics, 1974. **45**(10): p. 4436-4440.
39. Owsenek, B., J. Seyed-Yagoobi, and R. Page, *Experimental investigation of corona wind heat transfer enhancement with a heated horizontal flat plate.* Journal of Heat Transfer, 1995. **117**(2): p. 309-315.